Dependence of domain wall pinning potential landscapes on domain wall chirality and pinning site geometry in planar nanowires

L. K. Bogart and D. Atkinson*
Department of Physics, Durham University, Durham, United Kingdom, DH1 3LE

K. O'Shea, D. McGrouther, and S. McVitie
Department of Physics and Astronomy, University of Glasgow, Scotland, United Kingdom, G12 8QQ
(Received 21 November 2008; published 11 February 2009)

We report on domain wall pinning behavior and the potential-energy landscapes created by notches of two different geometries in planar Permalloy nanowires. Domain wall depinning was probed experimentally using spatially resolved magneto-optical Kerr effect measurements. The spin structure of pinned domain walls was determined using Lorentz microscopy, and domain wall pinning behavior was also analyzed using micromagnetic simulations, which are in good qualitative agreement with experimental results. All notch structures have dimensions that are comparable with the domain wall length scales. For the notch structures investigated, the depinning field experienced by a domain wall is found to be relatively insensitive to notch geometry although the pinning behavior is highly sensitive to both the wall type and the wall chirality spin structure. Energetically, the notches present both potential barriers and/or potential wells depending on the micromagnetic structure of the domain wall, and we find that the chirality of the domain wall is a key determinant of the pinning potential landscape. The pinning behavior of domain walls is discussed in detail, and direct quantitative measurements of the width and depth of the potential wells and/or barriers responsible for domain wall pinning are given for vortex walls pinned in triangular and rectangular notches.

DOI: 10.1103/PhysRevB.79.054414 PACS number(s): 75.60.Ch

I. INTRODUCTION

The pinning and propagation of domain walls (DWs) in planar nanowires has become the focus of intense research, with many proposed applications including both magnetic logic[1] and sensor[2] devices and more recently in magnetic memory concepts.[3,4] In such devices information is encoded in the magnetization direction of domains in planar nanowires, with the nucleation and propagation of DWs in nanowires allowing for the input, manipulation, and readout of stored information. Domain walls have been considered to behave as quasiparticles[5] that can be controlled by external magnetic fields, spin-polarized currents, and lithographically patterned variations in the nanowire geometry, such as notches. These structural features yield a pinning potential-energy landscape in which the quasiparticle can move under the action of a magnetic field and/or spin-polarized current, and by analogy with a mechanical oscillator the DW has been considered as a particle confined in a simple parabolic potential; the bottom of which is assumed to correspond to the physical center of the notch.[6] Detailed knowledge of the pinning potential created by different notches is a vital step toward understanding the fundamental properties of DWs, and also toward the optimization of DW pinning behavior that is required for magnetic memory devices.

The spin structure of a DW results from an energy minimization process that includes material-dependent properties as well as the local geometry of the nanowire. For magnetic materials with weak intrinsic anisotropies such as cobalt rich CoFe-based amorphous alloys or polycrystalline Permalloy nanowires (with a nominal composition around $Ni_{80}Fe_{20}$), the magnetization is largely constrained by magnetostatic energy considerations so as to lie along the long axis of the wire with spins parallel to the surfaces and edges. The magnetization direction in such magnetically soft nanowires is defined by the geometry of the nanowire, and when structural features such as notches are patterned within the nanowire, the spin structure tends to follow the local edges of these features. It was recently reported that different DW structures will experience different pinning interactions with a single triangular notch structure,[4,7–9] since the spin configuration through a structurally asymmetric feature presents different energetic barriers to a propagating DW depending upon the micromagnetic spin structure of the wall. This energetic difference manifests itself as a difference in the magnetic field required to push the wall through a structural pinning feature. As magnetostatic energy is dominant for materials with weak magnetocrystalline anisotropy and negligible magnetostriction, it is reasonable to suppose that varying the notch geometry will allow for modification of the DW potential-energy landscape, so we would expect a given wall structure to experience different pinning interactions depending on the geometrical structure of the notch. It is supposed, therefore, that structural pinning features—with different shapes but of comparable size to both each other and to the length scales of a DW within a planar nanowire—may present different energetic barriers to a propagating domain wall.

A precise understanding of how the domain wall potential-energy landscape is modified by different geometrical variations is currently lacking. In this study we report on the depinning of DWs from two notch geometries in planar Permalloy nanowires and show that, surprisingly, the potential-energy landscape of a notch is relatively insensitive to the notch structures and instead it is dependent upon the micromagnetic structure of the wall.

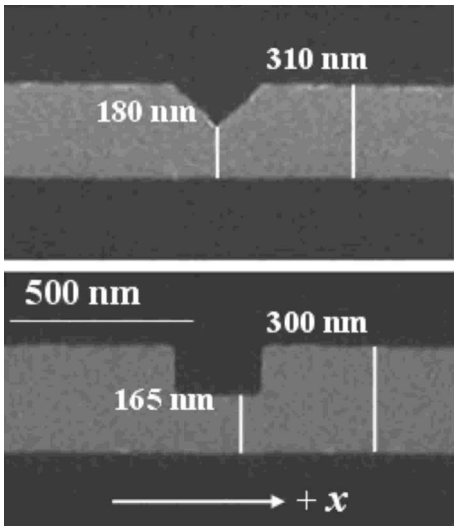

FIG. 1. Scanning electron micrograph images of a triangular and rectangular notch structures in a planar Permalloy nanowire. The nanowire structures were 10 nm thick and were fabricated by electron-beam lithography, thermal evaporation, and lift-off methods.

II. EXPERIMENTS

Planar magnetic nanowire samples of the same nominal dimensions were fabricated using electron-beam lithography followed by thin-film deposition and lift-off. The first sample was fabricated on a thermally oxidized silicon substrate, and the magnetic behavior was measured using spatially resolved magneto-optical Kerr effect (MOKE). Thin films were deposited by thermal evaporation from a single $Ni_{81}Fe_{19}$ source with a base pressure of 10^{-7} Torr and a growth pressure of 10^{-6} Torr at a rate of ~0.5 Å/s as measured by an *in-situ* quartz-crystal microbalance. In the second sample a thin film of $Ni_{81}Fe_{19}$ was deposited onto an electron transparent Si_3N_4 windowed substrate suitable for imaging in a transmission electron microscope (TEM).[10]

The nanowires were 10 nm thick and had a micron-scale DW nucleation pad on one end[11] and were sharply tapered at the other,[12] and contained a single notch pinning structure patterned along one side of the wire. The pinning structures were of two different geometries in the form of triangular and rectangular-shaped notches. In the first sample, the nanowires were 50 μm long, with the notch located approximately 25 μm from the nucleation pad, while in the second sample the nanowires were 10 μm in length. The dimensions of the notch structures were chosen to be comparable with the extent of the DW width using the definitions given in Ref. 13 so as to present an abrupt change to the potential-energy landscapes. We present detailed results for nanowires nominally 300 nm wide with notch structures of nominal depth approximately 50% of the wire width, as shown in Fig. 1.

Spatially resolved magnetization analysis was performed using a high-sensitivity longitudinal focused MOKE magnetometer utilizing a laser spot focused to an average width of 5 μm,[14] which allowed the magnetization reversal behavior of individual nanowire structures to be investigated locally, both before and after the pinning sites. This allowed the domain wall depinning fields to be quantified. MOKE measurements were performed using an alternating field at 23 Hz, and hysteresis loops were time averaged such that all loops represent many hundreds of field reversal cycles.

The differential phase contrast (DPC) mode of Lorentz microscopy[15] was used to investigate the detailed domain wall pinning interactions with the notches. This imaging technique was performed using a modified Philips CM20 FEG (Ref. 16) and is a scanning transmission electron microscope (STEM) technique in which the electron beam is focused to a probe and scanned across the sample. The electron beam emerges from the sample as a cone of illumination and is projected onto a circular quadrant detector. If a magnetic sample is placed in the path of the beam, the Lorentz force deflects the electrons and the emergent beam is not centered on the detector. This results in different signal levels from each of the four quadrants. By taking difference signals from opposite quadrants, pairs of images of orthogonal magnetic induction perpendicular to the electron trajectory are obtained. Further analysis of the image pairs yields a quantitative vector map of induction, illustrating the detailed form of the magnetic structure of interest.

Important insight into the relationship between DW structure and the pinning behavior was obtained using micromagnetic simulations performed using the OOMMF micromagnetic code.[17] All of the simulations utilized a 5 nm mesh and employed standard magnetic parameters for Permalloy including saturation magnetization $M_S=860\times10^3$ A/m, exchange energy constant $A=13\times10^{-12}$ J/m, and zero magnetocrystalline anisotropy. The simulations were performed in a quasistatic regime and were judged complete when the convergence criteria $|m\times h|\leq1\times10^{-5}$, with α set to 0.5 to speed up the simulations.

III. RESULTS

Figure 2 shows the MOKE hysteresis loops from (a) a 385 nm wide wire containing a triangular notch 190 nm deep and also (b) a 390 nm wide wire containing a rectangular notch 220 nm deep. We observe that each hysteresis loop contains two switching steps, which indicate that there are two principle depinning fields from each pinning structure. DWs were "injected" in the nanowires at 81 ± 2 Oe and 89 ± 2 Oe, respectively, as measured from MOKE hysteresis loops taken at the nucleation pad-wire interface. The first step, H_1, occurs at 95 ± 2 Oe for the triangular notch and 115 ± 2 Oe for the rectangular notch, while the second step occurs at 130 ± 2 Oe from both the triangular and rectangular notches. On the basis of micromagnetic energy considerations we would expect that the DW structure is a vortex wall (VW) (Ref. 18), and we suggest that these steps correspond to pinning interactions of the two vortex wall chiralities: clockwise (CW) and counterclockwise (CCW).

In Figs. 3 and 4 we present images of calculated vector induction distribution color maps, which show pinning of clockwise and counterclockwise VWs in triangular and rectangular notches, respectively. To aid interpretation a simplified schematic of the spin structure at each stage of the pin-

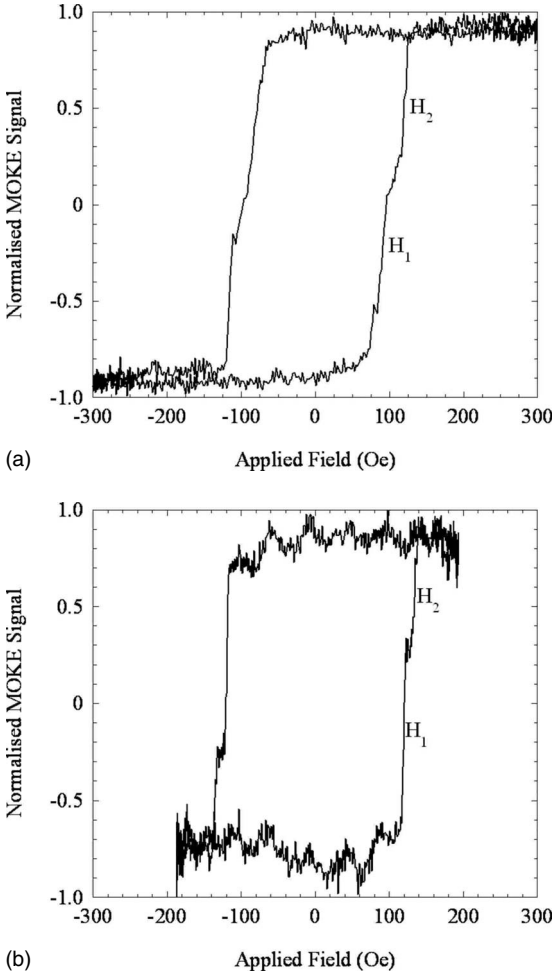

FIG. 2. MOKE hysteresis loops illustrating domain wall depinning from (a) a 190 nm deep triangular notch structure in a 385 nm wide wire and (b) a 220 nm deep rectangular notch structure in a 390 nm wide wire, respectively. There are two distinct switching fields present in each hysteresis loop which suggests there are two different domain wall depinning events occurring from each pinning site. Step H_1 occurs at an applied magnetic field of 95 ± 2 Oe in (a) and 115 ± 2 Oe in (b), while the step labeled H_2 occurs at 130 ± 2 Oe in both (a) and (b).

ning process is also presented. Head-to-head DWs are injected into the nanowires from a nucleation pad at approximately 12 Oe and are subsequently pinned at the notch. The applied field is then removed; Figs. 3 and 4 illustrate the form of the injected walls at remanence. The pinning interactions of both chiralities of VWs (chirality being the sense of magnetization rotation, or the handedness within the domain wall) in triangular notches are shown in Fig. 3. In Fig. 3(a), (I) and (II) are the DPC images of the x and y components of magnetic induction; (a) is the resulting induction color map, deduced from (I) and (II). In both (a) and (c) the injected wall is pinned in front of the notch, with the wall structures resembling that of a CW VW and CCW VW, respectively. In Fig. 3(a), the geometry of the leading edge of the notch allows the wall to compress to some extent into the notch as the magnetization in the wire directly below the notch is favorably aligned with the magnetization in the leading domain of the VW. In Fig. 3(c) the central wall section of the VW is aligned parallel with the edge of the notch, indicated by A, and the leading wall of the VW is pinned at the notch apex. As the applied magnetic field is increased along the positive x direction, the vortex core of the clockwise VW moves down toward the lower edge of the wire in (b) while the wall remains pinned at the leading edge of the notch and the wall width reduces noticeably. The wall abruptly depins at 18 ± 2 Oe. In the case of the counterclockwise VW, Fig. 3(d), at a field of 21 Oe the vortex core is no longer distinguishable and the wall appears transverse-like. The central wall section is now closer to the edge of the notch, however the wall does not extend beyond the apex of the notch. A significantly larger field of 31 ± 2 Oe is required to depin the counterclockwise VW from this notch.

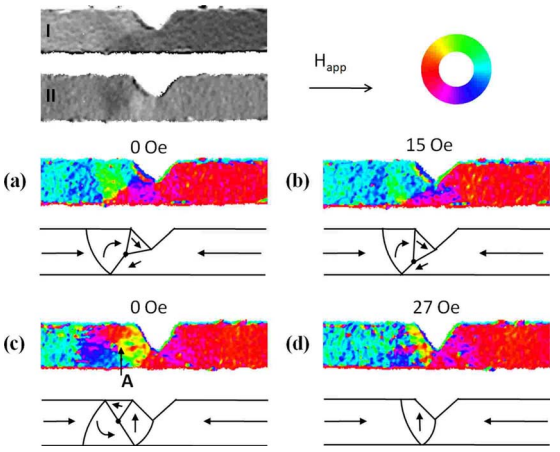

FIG. 3. (Color online) (I) and (II) are DPC images of the x and y components of magnetic induction, (a) is the color induction map deduced from (i) and (II). The images show vortex wall pinning in a triangular shaped notch, with (a) and (c) showing the domain wall pinned at remanence, while (c) and (d) illustrate the behavior as the magnetic field is increased.

DPC images of vortex walls pinned in rectangular notches are presented in Fig. 4. As in Fig. 3, parts (a) and (c) show

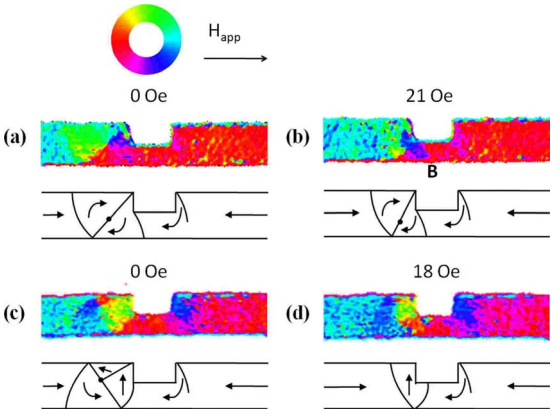

FIG. 4. (Color online) Color induction maps comparing the pinning location for a clockwise and counterclockwise vortex domain wall pinned in a rectangular-shaped notch. Images (a) and (c) show the domain wall pinned at remanence ahead on the left-hand side of the notch where it remains pinned and becomes compressed ahead of the notch as the magnetic field is increased in (b) and (d).

the injected DW at remanence. In both cases the wall is pinned on the left side of the notch, although the precise spin structure of each wall around the notch differs due to the local geometry. In Figs. 4(a) and 4(b) the abrupt edge of the notch prevents both vortex walls from entering the pinning site; in each case the leading wall of the VW is pinned at the first edge of the notch. As the applied magnetic field is increased, we see that in Fig. 4(b) the wall becomes significantly compressed although the geometry of the rectangular notch only allows for modest penetration of the leading edge of the wall into the notch at B. The CCW VW, Fig. 4(d), behaves in a similar manner in both rectangular and triangular notches under an applied field. At a field of 18 Oe the wall width compresses, whilst simultaneously forcing the vortex core out of the wire until the wall appears transverse-like. The depinning fields were similar for both wall types; a magnetic field of 24 ± 2 Oe was required to depin the clockwise VW, while the counterclockwise VW depinned at a field of 22 ± 2 Oe.

While the wall structure observed in the DPC imaging is in qualitative agreement with micromagnetic simulations (discussed later), the fields in the DPC imaging are consistently smaller by a factor of ~ 5 than both the micromagnetic simulations and the MOKE measurements. The reason for this discrepancy is not clear at present but may be related to material issues within the second sample or some perhaps unresolved discrepancy in the field calibration. The field values are presented here for completeness. The two wall chiralities display different pinning behavior, although for a given domain wall structure the behavior in each pinning site is very similar. It is suggested that the depinning events labeled H_1 and H_2 in Figs. 2(a) and 2(b) correspond to depinning events of specific wall chirality, although further analysis is required to identify which depinning event corresponds to which wall structure.

IV. DISCUSSION

In order to gain further insights into pinning behavior of VWs at these notch structures we have performed quasistatic micromagnetic simulations using the OOMMF software package. Using the phase diagram for domain wall structure in Ref. 18 as a guide, one of two basic DW states-up transverse wall (TW) or clockwise VW was artificially introduced in a rectangular shaped element 6000 nm long, with width w, and thickness t. [It is worthwhile noting that we have performed similar simulations for each wall structure of the opposite wall chirality (down TW and counterclockwise VW); although we do not present these results here, since in a symmetrical rectangular element the different chiralities of a given wall structure exist as energetically equivalent states.] The DW structure was then allowed to relax to its equilibrium configuration at zero-applied field. For each wire, a simulation was also performed at positive saturation, i.e., no DW. The energy of the DW, E^{DW}, was determined using Eq. (1), thereby accounting for both exchange and magnetostatic energies associated with the flat end shapes of the rectangular nanowire element. This energy value was then divided by the cross-sectional area of the planar nanowire, wt, to normalize all DW energies relative to one another,

$$E^{\mathrm{DW}} = E^{\mathrm{DW}}_{\mathrm{Total}} - E^{\mathrm{No\ DW}}_{\mathrm{Total}}. \quad (1)$$

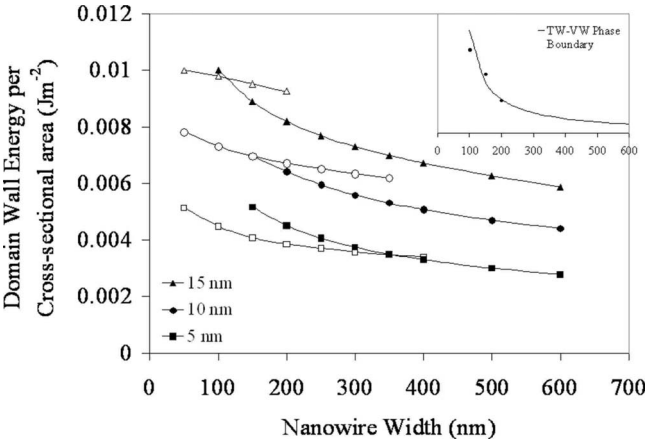

FIG. 5. Plot of domain wall energy per unit of cross-sectional area as a function of nanowire width, as deduced by quasistatic OOMMF micromagnetic simulations. Open symbols correspond to transverse walls while solid symbols correspond to vortex walls. The transverse-wall–vortex-wall phase transition deduced by Nakatani *et al.* (Ref. 18) is shown as an inset with a selection of data points for comparison.

In Fig. 5 we present results of DW energy per cross-sectional area as a function of wire width for head-to-head DWs. We have investigated nanowire widths between 50 and 600 nm and thicknesses from 5 to 15 nm inclusive. For each wire thickness we compare the energy per cross-sectional area for TWs and for VWs over a variety of wire widths. The first observation we make is that for a specific wall type in a wire of given width, the wall energy increases as the thickness increases; it is well known that the micromagnetic structure of a wall a nanowire can support is highly sensitive to the transverse dimensions of the wire.[19] At narrower wire widths the transverse wall structure has lower energy and thus is the favorable structure, whereas at larger wire widths the vortex wall is the lower energy and thus is the more favorable DW structure. Significantly, for each thickness investigated there is a considerable range of wire widths that can support both TWs and VWs with only small differences in energy. For example, at zero temperature a nanowire of cross-sectional dimensions 300×10 nm^2 a TW structure is only 16% higher energy than a VW, so although a VW is the favorable lowest energy state it is possible that at room temperature both DW structures can exist. The existence of multiple wall structures in wires of these dimensions is evidenced experimentally by the observation of different magnitudes of the measured AMR signal[7] and also in TEM imaging.[20] There is good quantitative agreement between our independent simulations and those of Nakatani[18] and McMichael and Donahue[19] (shown in the inset of Fig. 5), which adds confidence in using micromagnetic simulations for further analysis of domain wall pinning behavior at these pinning sites. The discrepancy between the DW energy values for 5 nm thick nanowires is explained by the existence of the asymmetric transverse wall (ATW) regime, which can be clearly seen in

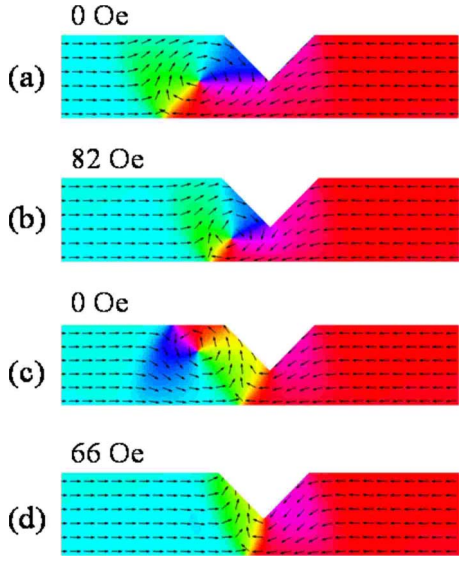

FIG. 6. (Color online) Micromagnetic simulations illustrating the pinning behavior of clockwise vortex domain walls (a) and (b) and counterclockwise domain walls (c) and (d) in a triangular notch structure as a function of magnetic field below the depinning field.

the inset. The ATW regime exists at thicknesses approximately 3 and 10 nm, up until wire widths of 400 nm, and our simulations show that in this regime (thin, wide wires) either wall type is favored.

We present micromagnetic simulations of vortex DWs pinned in triangular and rectangular notches in Figs. 6 and 7. All of the simulations utilized the initial static wall structures as used for the data in Fig. 5, and an applied field of 6 Oe to propagate the domain wall toward the notch. Once the DW was pinned at the notch the magnetic field was reduced to zero to simulate the DW pinning behavior from remanence

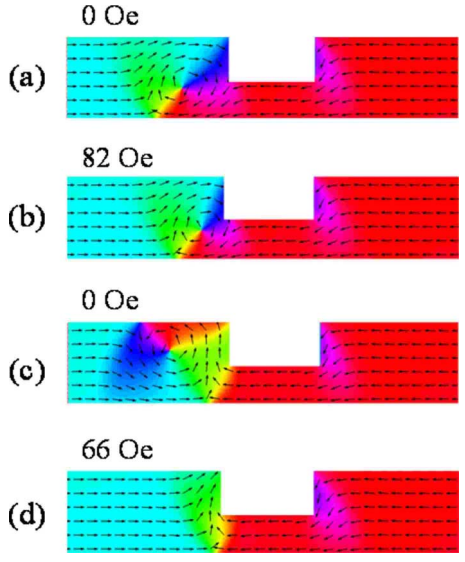

FIG. 7. (Color online) Micromagnetic simulations illustrating the pinning behavior of clockwise vortex walls (a) and (b) and counterclockwise vortex domain walls (c) and (d) in a rectangular notch structure as a function of magnetic field below the depinning field.

in the same manner as the TEM imaging in Figs. 3 and 4. The magnetic field was then increased in steps of 2 Oe in the positive x direction until the wall was completely depinned from the notch. Figures 6, 7(a), and 7(c) correspond to the DW pinned at remanence at the notch, while Figs. 6, 7(b), and 7(d) correspond to the pinned DW as it moves further into the notch as the applied magnetic field is increased.

Figure 6 closely reproduces what we experimentally observe in Fig. 3. At remanence, we see that both the CW and CCW VWs are pinned on the left-hand side of the notch. Considering the CW first, the leading edge of the vortex is seen to "anchor" itself to the apex of the triangular notch and that the core of the vortex is approximately level with the depth of the notch. As the applied magnetic field increases further in (b), the leading edge of the CW wall remains pinned in the same location (a), although we see that the wall width has appreciably narrowed. The vortex core moves slightly further down toward the bottom edge of the nanowire and the wall completely depins at an applied magnetic field of 84 Oe. The wall retains both its structure and chirality as it moves through and out of the pinning site. The pinning behavior of a CCW wall is noticeably different, and at remanance it is pinned at a location slightly further into the notch in (c) since the spins in the wire following the notch geometry are parallel to the spins in the leading edge of the wall. In this case the vortex core of the CCW is pushed from the middle of the wire and sits closer to the top of the wire, just as is observed in Fig. 3(b), and also looks quite asymmetric in character, which is expected due to the local geometry of the notch. As the applied magnetic field is increased further in the positive x direction the core of the CCW VW is pushed out of the wire resulting in the transformation of the VW to a TW, allowing the wall to move further into the notch, which also agrees very well with the TEM observations. This process occurs at a much higher field than the CW VW. The wall is strongly pinned in the triangular notch and is depinned at an applied magnetic field of 168 Oe.

Micromagnetic simulations for VW pinning in rectangular notches are shown in Figs. 7. For the CW VW we see that the leading edge of the vortex "anchors" itself to the first corner of the rectangular notch, and although the VW is slightly wider and more asymmetric than in Fig. 6(a) clockwise vortex walls interacts with each notch in a very similar manner. As the applied magnetic field increases further to (b) the wall remains pinned in the same location, although the wall width decreases significantly. The vortex core moves slightly further down toward the lower edge of the nanowire, and the wall completely depins at an applied magnetic field of 84 Oe as was the case for CW VW pinning in the triangular notch. Again, the wall retains its structure and chirality as it moves through and out of the pinning site. The pinning behavior of the CCW VW is also shown, and at remanence, (c) this wall structure is also pinned at the left-hand side of each notch structure, although it is more asymmetric than the clockwise VW at remenance. As the applied magnetic field is increased further we see that the core is pushed out toward the top of the wire, and the VW transforms to a TW, as seen in the TEM observations. The transformation to a TW occurs at very similar fields for the counterclockwise VW in both pinning structures and by transforming to a TW the energy is

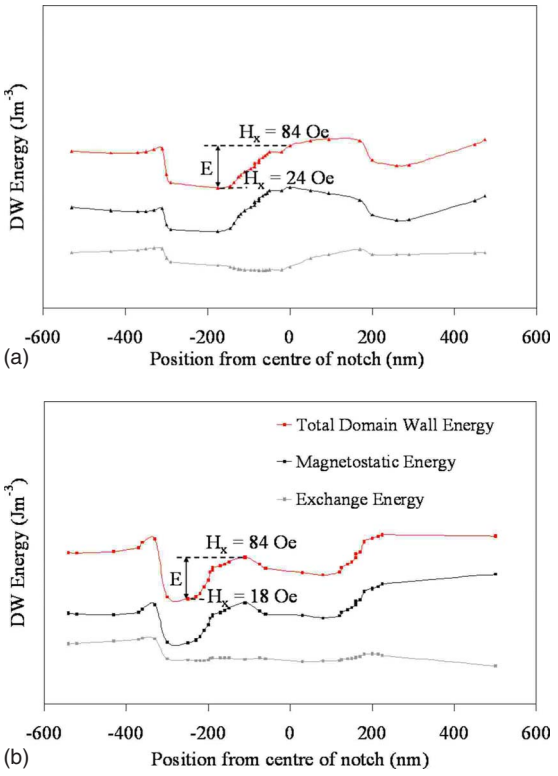

FIG. 8. (Color online) Domain wall pinning potential landscapes for clockwise vortex domain walls pinned in triangular (▲) and rectangular (■) notches as deduced from micromagnetic simulations. The constituent magnetostatic energy (black data points) and exchange energy (gray data points) of the DW are also shown, respectively.

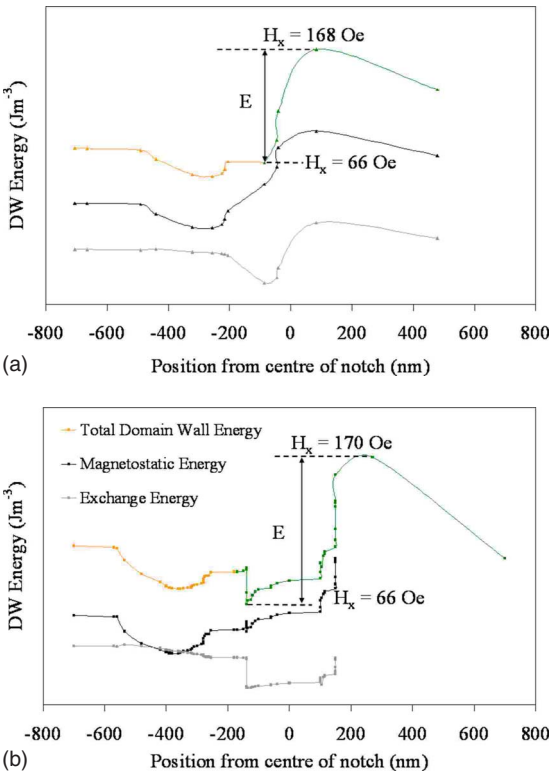

FIG. 9. (Color online) DW pinning potential landscapes for counterclockwise vortex domain walls pinned in triangular (▲) and rectangular (■) notches as deduced from micromagnetic simulations. The domain wall's constituent magnetostatic energy (black data points) and exchange energy (gray data points) are also shown, and we see that for this wall structure both energies are significant to the pinning behavior. As the domain wall moves into the narrow part of the notch it transforms to a transverse wall at a field around 66 Oe.

reduced. The wall is strongly pinned in the rectangular notch and is depinned at an applied magnetic field of 170 Oe.

For a triangular notch the micromagnetically modeled behavior is similar with higher pinning fields for CCW rather than CW head-to-head walls. However, it should be noted that the DPC imaging showed no difference in pinning fields for vortex walls from a rectangular notch for the single wire studied. The reason is not clear but the result is included for completeness. Although these fields are larger than what we measure in the TEM they are comparable to what we measure in the MOKE, and we attribute this to several reasons. All simulations were performed at zero temperature, and it is well known that the magnitude of the depinning field decreases as the temperature increase due to stochastic effects.[21] It is suggested the depinning fields measured in the MOKE may be influenced by thermal activation at room temperature in the measurements and/or perhaps by lithographic imperfections of the geometry of the real pinning structures.

The very good qualitative agreement between the micromagnetic simulations and the TEM observations gives us confidence to perform more sophisticated analysis of the energetics of DW depinning at these pinning site structures. Figures 8 and 9 present pinning potential-energy density landscapes derived from the micromagnetic simulations of clockwise and counterclockwise vortex walls shown in Figs. 6 and 7. The DW energy density, given in Eq. (2), is presented as a function of distance from the geometrical center of the notch, and accounts for changes in the DW energy as a result of compression in and around the notch,

$$U_{\mathrm{DW}} = E_{\mathrm{DW}} / V_{\mathrm{DW}}. \tag{2}$$

The volume of the wall is given by $\Delta_{\mathrm{wall}} \cdot w \cdot t$. The energy density of the DW at each position is defined using Eq. (3), which removes the Zeeman (field) energy and accounts for any energy associated with spin structure localized to the notch in the absence of a domain wall and also due to the end effects,

$$U^{\mathrm{DW}} = (U^{\mathrm{DW}}_{\mathrm{Total}} - U^{\mathrm{DW}}_{\mathrm{Zeeman}}) - (U^{\mathrm{No\ DW}}_{\mathrm{Total}} - U^{\mathrm{No\ DW}}_{\mathrm{Zeeman}}). \tag{3}$$

The DW position is defined as the distance of the vortex core to the center of the pinning site structure. When the VW transforms to a TW then the apex of the TW is defined as the central position of the DW.

In Fig. 8 we present pinning potential landscapes for clockwise vortex domain walls pinned in triangular (▲) and rectangular (■) notches, deduced from micromagnetic simulations. The constituent magnetostatic energy (black data points) and exchange energy (gray data points) of the DW are also shown, and for this wall structure the magnetostatic

energy dominates the overall pinning behavior. The DW is initially repelled from each notch structure as seen by the small local potential barrier at approximately $x=-400$ nm, but once the wall overcomes this repulsion each notch presents an attractive potential well. A potential well is a local minimum in potential energy, while a potential barrier is defined as a local maximum in potential energy. The center of this potential well is located approximately 200 nm from the geometrical center of the notch. The clockwise vortex wall is depinned from each notch at a magnetic field of 84 Oe, with the second dip simply due to the domain wall re-arranging spins as it moves through and beyond the narrow part of the notch. The height of the well is defined as E, and is the energy that the wall must acquire to depin. This is calculated by multiplying the energy density U by the volume of the wall ($\Delta_{\text{wall}} \cdot w \cdot t$) when it is at the bottom of the potential well, i.e., the stable location before it depins from the notch. This is deduced to be 1.46 and 1.79 eV for the triangular and rectangular notches, respectively.

Figure 9 presents DW pinning potential landscapes for CCW VWs pinned in triangular (▲) and rectangular (■) notches. The constituent magnetostatic energy (black data points) and exchange energy (gray data points) of the DW are also shown and in this case both energies are significant to the pinning behavior. As the DW moves into the narrow part of the notch it transforms to a transverse wall. The DW is initially attracted to each notch structure as seen by the small potential well between $x=-400$ nm and $x=-200$ nm, but once the wall overcomes this repulsion each notch presents a large potential barrier in which both exchange and magnetostatic energies have significant contributions. The center of this well is located approximately in the physical center of the notch, and the wall is depinned from each notch structures at an applied magnetic field of 168 and 170 Oe, correspondingly. The energy barrier that the domain wall must overcome is deduced as 2.30 and 2.63 eV from the triangular and rectangular notches, respectively

In each figure it can be seen that pinning potential profiles are primarily determined by the micromagnetic structure of the domain wall, with the specific geometry of the notch of secondary importance to the potential-energy landscape. Figures 8 and 9 show that the pinning potential landscape is very similar for each chirality of vortex wall as it propagates toward and depins from each notch structure, although the two wall chiralities experience very different landscapes to each other when pinned in the same notch geometry. Both triangular and rectangular notches can act as either potential wells or potential barriers, and that this is determined by the spin structure of the propagating domain wall. The pinning potential landscapes are much more detailed than what has been previously reported in the literature.

V. CONCLUSION

A combination of MOKE magnetometry, Lorentz microscopy, and OOMMF micromagnetic simulations has allowed for a systematic study into the dependence of the domain wall pinning behavior on the domain wall chirality at two pinning site structures. We have shown previously that pinning site saturation occurs when the notch depth to wire width ratio exceeds approximately 0.6 (Ref. 9) and in this work we have observed that when pinning sites are comparable in size to the DW width then the detailed geometry of the notch is of secondary importance to the domain wall depinning field for a given domain wall structure will experience very similar depinning fields from both triangular and rectangular notches of the same depth and width. The spatial extent of the potential well is found to extend far beyond the physical size of the notch due to the finite size of the domain wall. Each notch structure is seen to act as either an attractive potential well or as a potential barrier depending on the structure of the DW that is interacting with the notch, and similar work has been reported for DW pinning in antinotches.[22] If we are interested in using DWs in magnetic memory devices then it is important that we have a comprehensive characterization of the pinning site potential landscape, and our results show that DW pinning behavior is complicated.

*del.atkinson@durham.ac.uk

[1] D. A. Allwood, G. Xiong, C. C. Faulkner, D. Atkinson, D. Petit, and R. P. Cowburn, Science **309**, 1688 (2005).
[2] M. Diegel, R. Mattheis, and E. Halder, IEEE Trans. Magn. **40**, 2655 (2004).
[3] S. S. P. Parkin, U.S. Patent No. 6,834,005 (16 December 2004); S. S. P. Parkin, U.S. Patent No. 6,898,132 (16 December 2004); S. S. P. Parkin, U.S. Patent No. 6,920,062 (14 April 2005); S. S. P. Parkin, U.S. Patent No. 7,031,178 (5 May 2005); S. S. P. Parkin, U.S. Patent No. 7, 236,386 (8 June 2006).
[4] D. Atkinson, D. S. Eastwood, and L. K. Bogart, Appl. Phys. Lett. **92**, 022510 (2008).
[5] M. Klaui, J. Phys.: Condens. Matter **20**(31), 313001 (2008).
[6] S. S. P. Parkin, M. Hayashi, and L. Thomas, Science **320**, 190 (2008).
[7] M. Hayashi, L. Thomas, C. Rettner, R. Moriya, X. Jiang, and S. S. P. Parkin, Phys. Rev. Lett. **97**, 207205 (2006).
[8] D. Petit, A.-V. Jausovec, D. Read, and R. P. Cowburn, J. Appl. Phys. **103**, 114307 (2008).
[9] L. K. Bogart, D. S. Eastwood, and D. Atkinson, J. Appl. Phys. **104**, 033904 (2008).
[10] M. Ruhrig, B. Khamespour, K. J. Kirk, J. N. Chapman, P. Aitchison, S. McVitie, and C. D. W. Wilkinson, IEEE Trans. Magn. **32**, 4452 (1996).
[11] R. P. Cowburn, D. A. Allwood, G. Xiong, and M. D. Cooke, J. Appl. Phys. **91**(10), 6949 (2002).
[12] K. J. Kirk, J. N. Chapman, S. McVitie, P. R. Aitchison, and C. D. W. Wilkinson, Appl. Phys. Lett. **75**, 3683 (1999).
[13] L. Thomas and S. S. P. Parkin, in *Handbook of Magnetism and Advanced Magnetic Materials*, edited by H. Kronmüller and S. S. P. Parkin (Wiley, Chichester, 2007), Vol. 2, pp. 942–982.
[14] D. A. Allwood, G. Xiong, M. D. Cooke, and R. P. Cowburn, J.

Phys. D **36**, 2175 (2003).
[15] J. N. Chapman, J. Phys. D **17**, 623 (1984).
[16] J. N. Chapman, A. B. Johnston, L. J. Heyderman, S. McVitie, and W. A. P. Nicholson, IEEE Trans. Magn. **30**, 4479 (1994).
[17] http://math.nist.gov/oommf/.
[18] Y. Nakatani, A. Thiaville, and J. Miltat, J. Magn. Magn. Mater. **290-291**, 750 (2005).
[19] R. D. McMichael and M. J. Donahue, IEEE Trans. Magn. **33**, 4167 (1997).
[20] D. Atkinson and S. McVitie (private communication).
[21] A. Himeno, T. Okuno, T. Ono, K. Mibu, S. Nasu, and T. Shinjo, J. Magn. Magn. Mater. **286**, 167 (2005).
[22] K. J. O'Shea, S. McVitie, J. N. Chapman, and J. M. R. Weaver, Appl. Phys. Lett. **93**, 202505 (2008).